2023 IEEE/ASME International Conference on Advanced Intelligent Mechatronics (AIM)
June 28-30, 2023. Seattle, Washington, USA

Proposal of On-board Camera-Based Driving Force Control Method for Autonomous Electric Vehicles

Takumi Ueno[1], Hugo Pousseur[2], Binh Minh Nguyen[3], Alessandro Correa Victorino[4], and Hiroshi Fujimoto[5]

***Abstract*—By utilizing the camera installed in the front of a vehicle, this paper proposes on-board camera-based driving force control (CDFC) methods for autonomous electric vehicles driven by in-wheel motors. The image processing algorithm can detect the change in road surface conditions quickly and accurately. This enables the CDFC to update the slip-ratio limiter in real-time. Test results show that the proposed methods can improve traction control performance and reduce inverter input energy.**

***Index Terms*—Automotive system, Driving force control, Electric vehicle, Image processing, Motion control**

I. Introduction

Due to the increasing awareness of global warming and energy resource limitations, electric vehicles (EVs) have been getting much attention. EVs are superior not only in terms of transportation but also in vehicle motion control. For instance, EVs' torque response is faster and more accurate than that of internal combustion engine vehicles. Especially the in-wheel-motors (IWMs) allow the EVs to control the torque at each wheel independently. It also has a relatively high bandwidth since no drive shaft is required.

Thanks to the merits mentioned above, various studies have been conducted using the IWM-EVs [1]–[6], including the research on autonomous driving cars [3]–[6]. The following fundamental issues should be solved to realize autonomous in-wheel-motor electric vehicles (AIWM-EVs). First, knowing the environment is an essential task because it allows the control of the vehicle [7] and makes driving safer. Second, developing the traction control system is essential, which can effectively integrate with other motion control layers in the autonomous driving system. However, no study deals with the above issues simultaneously and systematically.

Through the literature review, traction control of IWM-EVs can be organized into three main groups. The first group is anti-skid control (ASC) based on disturbance observer [8], [9]. The second group is slip ratio control (SRC), which can be realized by various techniques such as proportional-integral control [8], linear quadratic regulator [10], fuzzy logic control [11], model predictive control [12], and sliding mode control [13]. The last group is driving force control (DFC), which can be designed with a cascade configuration: the outer loop controls the driving force, and the inner loop controls the wheel's rotational speed [14], [15]. Although ASC is simple to be implemented, it is merely a rough traction control. Thanks to IWM-EVs' capability to accurately generate the driving force at each wheel, the DFC is the best candidate for AIWM-EV. However, the following issue still needs to be concerned. Almost the DFC and traction control methods cannot quickly detect road conditions. Road friction is one of the most important environmental parameters. It should be known to update the slip ratio boundary, which calculates the reference wheel speed in the DFC. Some road friction and driving stiffness estimation methods have been proposed [16], [17]. However, they are merely based on the motion sensors such as the wheel encoder and accelerometer. The change in the road condition only reflects on such sensors as the vehicle enters the new road surface. Due to sensor noises and model uncertainties, the existing methods always suffer from the estimation values' latency. In other words, the vehicle cannot instantly detect the road condition change, but after a specific time. Such latency might degrade traction control performance and result in extra energy consumption of the EVs.

For the above discussion, this paper aims to develop new DFC methods for AIWM-EVs by utilizing a camera, which is commonly equipped in the autonomous driving system.

The camera is increasingly used to detect the environment surrounding the ego vehicle. This evolution is due to the progress of image processing, allowing information acquisition by analyzing the camera's images. This information can be various, not only of lanes, obstacles, vehicles, and pedestrians but also the friction of the road. In this paper, we perform image processing from the camera installed in the front of the vehicle to estimate the friction coefficient of the road surface. In the literature, several articles deal with this road friction estimation problem. These papers start from the same method: to detect the type of surface using image processing tools combined with machine learning or deep learning methods [18], [19]. These models, combined with knowledge, allow the estimation of the road friction coefficient. These models use a camera's data to classify the type of road by exploiting only the camera's image [20]. The arrival of deep learning and, more particularly, of convolution neural network (CNN) [21] allows for realizing more precise classifications and being able to realize predictions in complex situations (for example, bad weather, weak contrast). However, this power gain reduces the execution speed of the model and requires more resources [22]. For this reason, we perform a surface-type prediction using traditional image preprocessing methods to reduce the computation time and thus obtain a fast detection adapted to the controller computation time. Our approach performs classification by filtering pixels close to a reference color. Once the nature of the road is detected in the image, the friction coefficient estimation can be determined using knowledge

[1] ueno.takumi22@ae.k.u-tokyo.ac.jp,
[2] hugo.pousseur@hds.utc.fr,
[3] nguyen.binhminh@edu.k.u-tokyo.ac.jp,
[4] alessandro.victorino@hds.utc.fr,
[5] fujimoto@k.u-tokyo.ac.jp

(relation between the road surface and coefficient friction) and optical geometry [23]. The estimated value is used to update the slip ratio limiter of the DFC, which allows the vehicle to run without tires' slippage and reduce inverter input energy on the low friction surface. Thus, the new method is named on-board camera-based driving force control (CDFC).

The remainder of this paper is organized as follows. The vehicle model is presented in Section II. The image processing algorithm is presented in Section III, followed by the proposed CDFC in Section IV. Experimental evaluations are presented in Section V. Finally, the conclusions are stated in Section VI.

II. Vehicle Model

As shown in Fig. 1(a), the rotational motion of the wheel and the longitudinal motion of the vehicle body can be described as

$$J\dot{\omega}_i = T_i - rF_{d,i} \tag{1}$$

$$M\dot{V}_{x,i} = \sum F_{d,i} \tag{2}$$

where J is the wheel moment of inertia, ω is the wheel angular velocity, T is the motor torque, r is the wheel radius, F_d is the driving force, M is the vehicle mass, V_x is the longitudinal velocity, and the subscription i denotes the wheel index. The slip ratio can be described as

$$\lambda_i = \frac{(V_{\omega,i} - V_{x,i})}{\max(V_{\omega,i}, V_{x,i}, \epsilon)} \tag{3}$$

where $V_\omega = r\omega$ and ϵ is a small positive value to prevent division by zero. The relationship between the road friction coefficient μ and slip ratio is shown in Fig. 1(b). It is commonly described by Pacejka's magic formula [24]:

$$\mu_i = D\sin[C\arctan(B\lambda_i - E(B\lambda_i - \arctan(B\lambda_i)))] \tag{4}$$

where B, C, D, and E are the fitting values obtained by the experiments. When the slip ratio is relatively small, the friction coefficient is approximately proportional to the slip ratio. By using the driving stiffness D_s, the driving force can be linearized as

$$F_{d,i} = D_{s,i}\lambda_i. \tag{5}$$

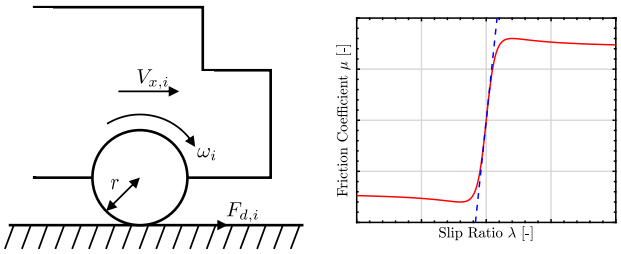

(a) Vehicle model. (b) μ–λ curve.

Fig. 1: Vehicle and tire model

III. Image Processing

A. Problem setting of this paper

This section is to acquire information about the type of road surface to deduce the friction coefficient.

In our experiments, wet blue polymer sheets simulate the low friction surface. The "blue-sheet" defines this surface in the rest of this paper. In order to detect the type of surface, our solution classifies each pixel of our image into three classes: ROAD, UNKNOWN, and BLUE.

B. Process algorithm

As explained in III-A, we need to set up a process to detect the presence of blue-sheet. In this way, we can deduce the type of surface on which the vehicle drives. This detection performs a membership test and estimates the type of road for each pixel. The role process is structured in 5 steps, illustrated by Fig. 2(a), as described below:

1) **select region of interest (ROI)**: select an area in which the process will apply, removing useless parts (like the sky);
2) **compute distance to reference color**: the distance between pixels color and color reference is computed (norm 2);
3) **filter distances**: based on the distance calculated in the previous step, only distances less than ϵ are selected as true;
4) **reduce image**: reduction of the binary image to reduce the computation time of the next steps;
5) **apply confidence mask**: application of a confidence mask in order to avoid error propagation from bad detection;

Fig. 2(b) shows the result obtained after the image processing application. The output image is described by a matrix, such that each coefficient (u, v) of this matrix represents the predicted class weighted by a confidence level between 0 and 100. Here, the class belongs to {road, blue-sheet}. Pixels in the center of the ROI have a higher confidence level than pixels at the edge. The allocation of a confidence coefficient can correct two problems; firstly, the color is not perceived as the same color if the object is far away, and second, the world projection of an object too far away is inaccurate. A value close to 0 means that the prediction considers this position unknown.

C. Surface grid map

Once this detection is done, the information must be kept to use when the vehicle is above this zone. The idea is to create a grid on which the information of the type of surface from the prediction performs in the image frame.

1) Image Frame to 3D world: From the position of a pixel in the image (u, v), it is possible to deduce its position in the camera space based on the intrinsic parameters of the camera, focal length (f_x, f_y), and optical center (c_x, c_y). In addition to the intrinsic data, we need to know the relationship between the vertical position of this pixel (v) and the distance between

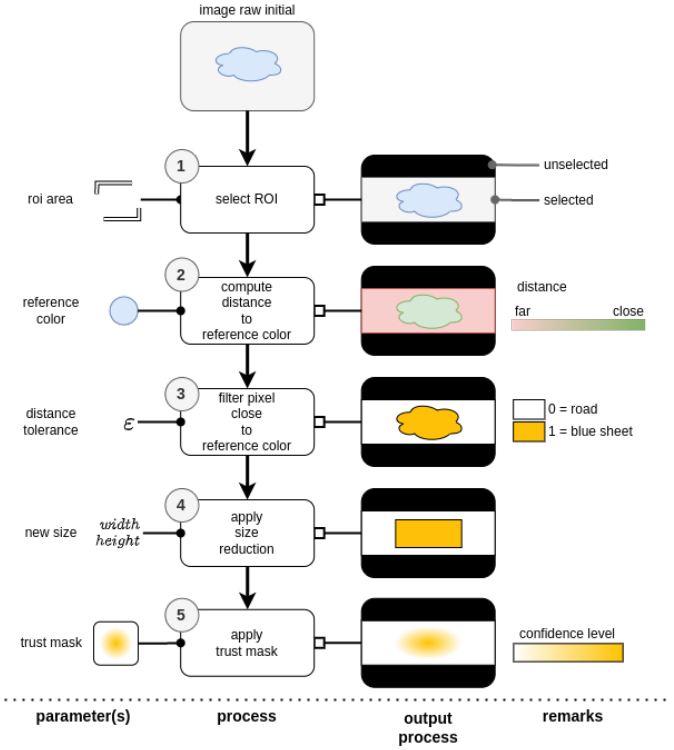

(a) Illustration of the image processing pipeline, showing the process hyperparameters.

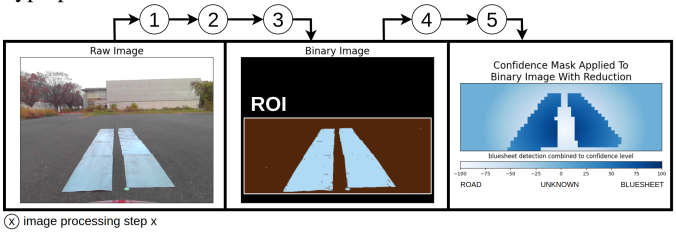

(b) Result obtained by applying image processing steps.

Fig. 2: Figures illustrate the process described in the section III-B.

the camera (z_c) and the real object represented by this pixel. This relation ($z_c = z(v)$) is obtained by calibrating two points whose vertical position in the image and actual distance are known. The position, in the camera frame, of the pixel is then defined as

$$x_c = \frac{u - c_x}{f_x} z(v) \tag{6}$$

$$y_c = \frac{v - c_y}{f_y} z(v). \tag{7}$$

Knowing the camera's extrinsic parameters and the vehicle's position with a GPS (x_r, y_r), it is possible to project this position in the world reference frame. Obtaining, the final transformation $(u, v) \xrightarrow{(x_r, y_r)} (x_w, y_w, z_w)$ describing the position in the world frame.

2) Surface Road Grid: Detected information is saved in a grid called "Surface Road Grid." Once the road surface information is detected and projected from the image frame to the world frame, the grid should be updated with the new information. This grid is updated with each new detection, keeping the previous information, which reduces the risk of bad detections. The surface grid is defined by a matrix $G \in \mathcal{M}_{M,N}([-1, 1])$. The cell value reflects the type of surface, -1 for "road" and 1 for "blue-sheet", weighted by a confidence coefficient. To construct this grid, one grid is defined per class, $B \in \mathcal{M}_{M,N}(\mathcal{B})$ for the blue-sheet surface and $R \in \mathcal{M}_{M,N}(\mathcal{R})$ for the road surface. As described above, each pixel from the image camera is defined by a position and surface prediction. The idea is to project this information in this grid using the position of the vehicle (x_r, y_r) and grid settings, size and resolution (s, r). Thus, pixel at position (u, v) can be projected as

$$(u, v) \xrightarrow{(x_r, y_r)} (x_w, y_w, z_w) \xrightarrow{(s,r)} (i, j) \tag{8}$$

where (i, j) defines the position in the grid. According to the prediction made per pixel, the layer of the predicted class is updated as

$$\begin{cases} R_{ij} = R_{ij} + \hat{p}_{uv} & \text{if } \hat{p}_{uv} < 0 \\ B_{ij} = B_{ij} + \hat{p}_{uv} & \text{if } \hat{p}_{uv} > 0. \end{cases} \tag{9}$$

Thus the final grid is defined as

$$G_{ij} = \begin{cases} \frac{B_{ij} + R_{ij}}{|B_{ij}| + |R_{ij}|} & \text{if } |B_{ij}| + |R_{ij}| \neq 0 \\ 0 & \text{else.} \end{cases} \tag{10}$$

In this way, the value of each grid cell is normalized between [-1,1]; a value close to -1 represents a road surface, and a value close to 1 represents a blue-sheet surface.

IV. Proposal of the Control System

In this section, the camera-based driving force control is proposed. Figures 3(a) and 3(b) show the block diagram of the CDFC-1 and CDFC-2, respectively. Fig. 4 shows the block diagram of the DFC. They are developed by a cascade configuration. Note that the total driving force command F^*_{all} is given by the autonomous control layer, which is not necessary to be presented here. The outer loop has a driving force controller C_F, and the inner loop has a wheel speed controller C_ω. In this paper, C_F is an integral controller (I), and C_ω is a proportional–integral controller (PI). In the outer loop, the driving force observer (DFO) utilizes the motor torque and angular velocity to provide the estimated F_d. The output of C_F is y_i, which is approximately the slip ratio in either acceleration and deceleration situation and defined as

$$y_i = \frac{V_{\omega,i}}{V_{x,i}} - 1. \tag{11}$$

In addition, we set the limiter of $y_{max,i}$ to prevent excessive slippage and defined it as

$$y_{max,i} = \frac{\hat{\mu}_i F_{z,i}}{\hat{D}_{s,i}} \tag{12}$$

where the value of $\hat{\mu}_i$ and $\hat{D}_{s,i}$ can be obtained as follows. Preliminary tests were conducted in both CDFC-1 and CDFC-2 to

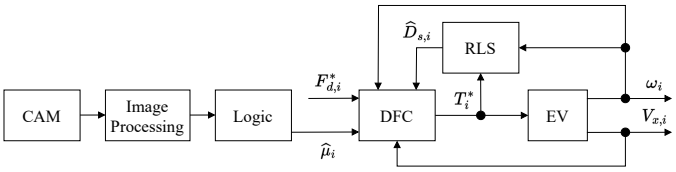

(a) CDFC-1.

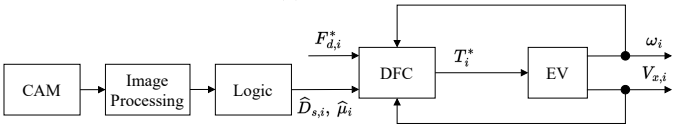

(b) CDFC-2.

Fig. 3: Block diagram of the proposed CDFC.

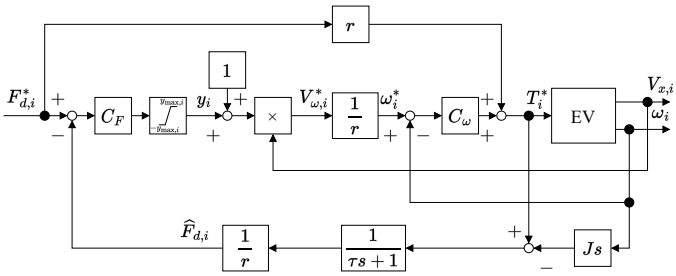

Fig. 4: Block diagram of the driving force controller.

identify the $\hat{\mu}_i$ value on the different road surfaces. Based on the image processing result, simple logic can be implemented: IF image$\{x_\omega, y_\omega, z_\omega\}$ is $\#$ THEN $\hat{\mu}_i\{x_\omega, y_\omega, z_\omega\} = \mu_\#$ where $\#$ belongs to the set of $\{$ROAD, BLUE$\}$ in this study. For comparison, CDFC-1 updates $\hat{D}_{s,i}$ via a recursive least square (RLS) algorithm based on Eq. (5) [14]. On the other hand, CDFC-2 updates the driving stiffness via the logic mentioned above: IF image $\{x_\omega, y_\omega, z_\omega\}$ is $\#$ THEN $\hat{D}_{s,i}\{x_\omega, y_\omega, z_\omega\} = D_{s,i\#}$. In addition, the vertical load on tire $F_{z,i}$ can be calculated from the gyroscope and accelerometer.

V. Experimental Evaluation

Section III presents the surface grid generation; the information must be adapted to the controller. The first step is to create the road profile for each side of the vehicle (right and left) from the grid. This profile describes the local road profile by a one-dimensional representation, where x is the distance, $P_k(x)$ the road profile, and side k, at a distance x. For any positions l, given in the world (x_l, y_l), we can estimate this position in the grid: (i_l, j_l), we note T the application performing this transformation. From this position, we can deduce the type of surface using the grid map surface, $G_{i_l j_l}$. We note G the application, such as $G(i,j) \rightarrow G_{i,j}$. Thus, we can deduce the profile as follows:

$$P_k(x) = G(T(x_r + x\cos(\theta_r),\ y_r + x\sin(\theta_r) \pm L)) \quad (13)$$

where (x_r, y_r) denotes the current vehicle position in the world frame, θ_r the current vehicle heading angle, and L the distance from gravity center to driving wheel side axis (left: $-L$, right: $+L$). Knowing the mapping between the surface type and the friction coefficient, $\mu_{map} : \{-1, 1\} \rightarrow \{\mu_{road}, \mu_{bluesheet}\}$, the friction profile, side k, is defined by the relation, $P_k^\mu(x) = \mu_{map}(P_k(x))$.

TABLE I: VEHICLE SPECIFICATIONS

Symbol	Description	Value
M	Vehicle Mass	$925\,\mathrm{kg}$
r	Effective wheel radius	$0.302\,\mathrm{m}$
J	Inertia of wheel	$1.26\,\mathrm{kgm}^2$

A. Experimental setting

Fig. 5(a) shows the experimental vehicle, FPEV-2 Kanon, developed by Fujimoto Lab. The vehicle is a four-wheel drive system with IWMs and is powered by a lithium-ion battery. In this paper, we use the vehicle as a rear-drive system. The main parameters are shown in Tab. I. Fig. 5(b) shows the road friction change scenario. The experimental scenario is as follows. The vehicle goes straight on high friction roads and, from the $0.5\,\mathrm{s}$, enters low friction roads simulated by polymer sheets sprinkled with water with the constant torque $200\,\mathrm{Nm}$. Under this condition, three test cases are conducted; 1. Without control, 2. With CDFC-1, 3. With CDFC-2. Assuming that the information on the road surface is known from the camera, this information is used to calculate y_{max}. $\hat{\mu}$ of high and low friction road in CDFC-1 and CDFC-2 is set $\mu = 0.8$ and $\mu = 0.2$, respectively. In addition, in CDFC-2, the controllers were set D_s as $25\,000\,\mathrm{Nm}$ ($\mu = 0.8$) and $4000\,\mathrm{Nm}$ ($\mu = 0.2$), respectively. In the DFC, the integral gain of C_F is set at 0.003, and the integral and proportional gains of C_ω are 50.476 and 504.76, respectively.

B. Experimental result

Figures 6, 7, and 8 show the result of the driving force, slip ratio, and longitudinal velocity in each experiment. These figures show that the CDFCs can maintain higher driving forces than that without control. In addition, when entering the low friction surface, the change of slip ratio of CDFC-2 is faster than that of CDFC-1. This is because the RLS algorithm takes a little time to estimate. To evaluate the effectiveness of the two proposed methods, the energy needed when the vehicle runs on the low friction road of each controller is shown in Fig. 9. It shows that the CDFC-1 and CDFC-2 can reduce the inverter input energy by $36.8\,\%$ and $24.0\,\%$, respectively, compared with the case without control. In addition, the reason that the energy of CDFC-2 is lower than CDFC-1 is due to the setting of the driving stiffness on high-friction and low-friction roads.

VI. Conclusion

This paper proposes two on-board camera-based DFC methods for the autonomous driving of electric vehicles. The key idea is to update real-time slip ratio limiters in the DFC using camera image processing. The experimental result shows the effectiveness of the proposed system. Compared with the case without control, the CDFCs can suppress excessive slippage and reduce the inverter input energy. In the future, we will

(a) FPEV-2 Kanon.

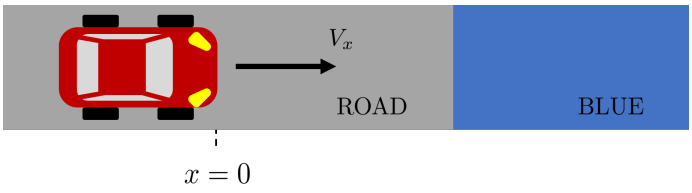

(b) Road friction change scenario.

Fig. 5: Experimental setup.

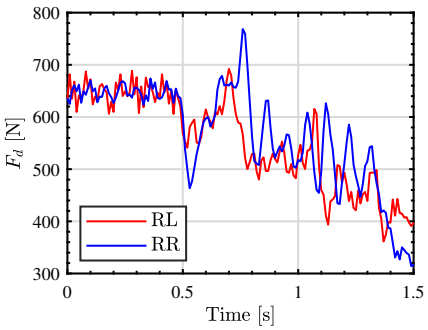

(a) Driving force.

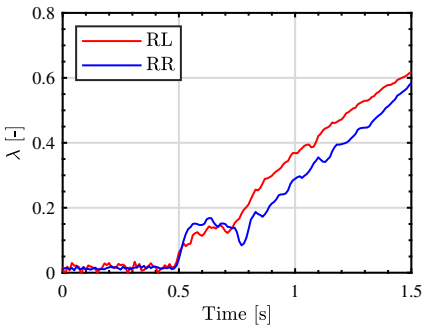

(b) Slip ratio.

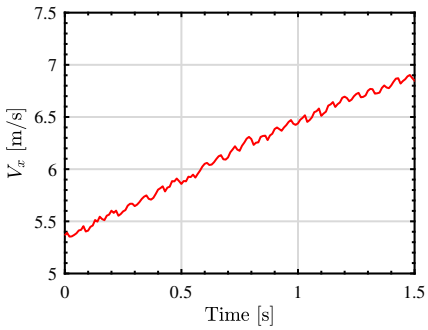

(c) V_x.

Fig. 6: Experimental result without control.

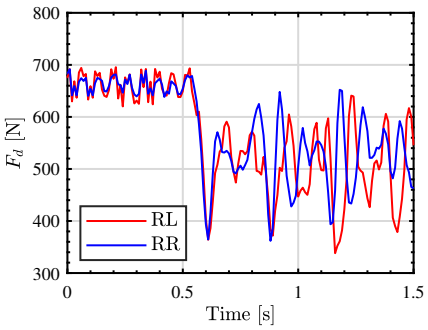

(a) Driving force.

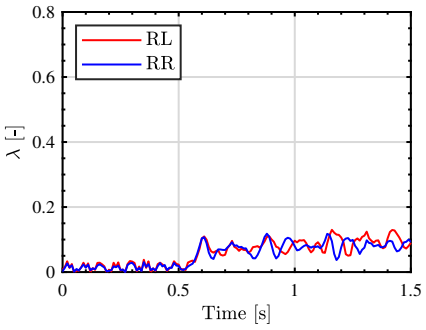

(b) Slip ratio.

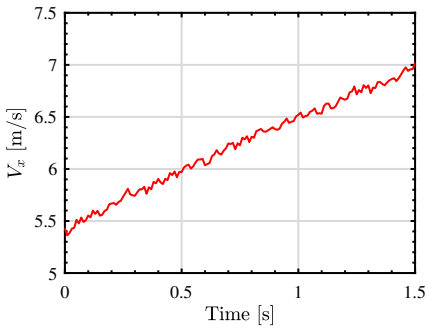

(c) V_x.

Fig. 7: Experimental result with CDFC-1.

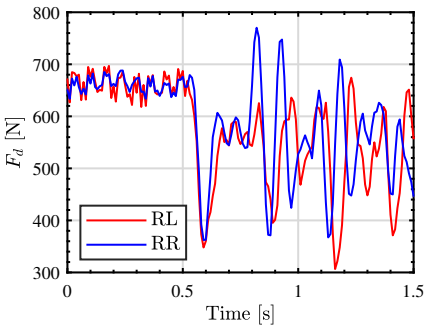

(a) Driving force.

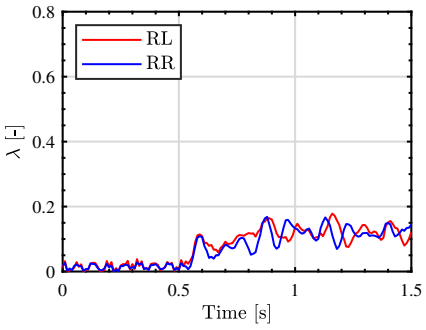

(b) Slip ratio.

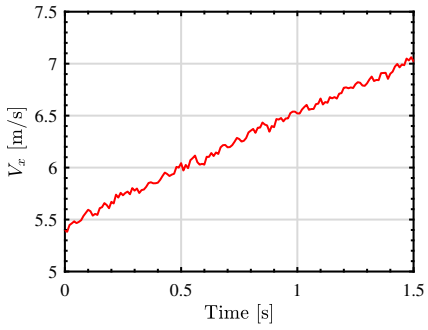

(c) V_x.

Fig. 8: Experimental result with CDFC-2.

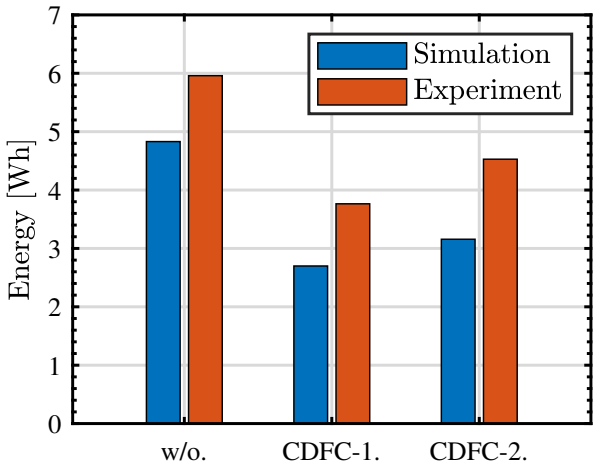

Fig. 9: Inverter input energy.

conduct further experiments in which the right and left wheel's road conditions are different.

REFERENCES

[1] E. Hashemi, M. Jalali, A. Khajepour, A. Kasaiezadeh, and S.-k. Chen, "Vehicle stability control: Model predictive approach and combined-slip effect," *IEEE/ASME Transactions on Mechatronics*, vol. 25, no. 6, pp. 2789–2800, 2020.

[2] M. Dalboni, D. Tavernini, U. Montanaro, A. Soldati, C. Concari, M. Dhaens, and A. Sorniotti, "Nonlinear model predictive control for integrated energy-efficient torque-vectoring and anti-roll moment distribution," *IEEE/ASME Transactions on Mechatronics*, vol. 26, no. 3, pp. 1212–1224, 2021.

[3] Y. Ikezawa, H. Fujimoto, Y. Hori, D. Kawano, Y. Goto, M. Tsuchimoto, and K. Sato, "Range extension autonomous driving for electric vehicles based on optimal velocity trajectory generation and front-rear driving-braking force distribution," *IEEJ Journal of Industry Applications*, vol. 5, no. 3, pp. 228–235, 2016.

[4] Y. Huang, F. Wang, A. Li, Y. Shi, and Y. Chen, "Development and performance enhancement of an overactuated autonomous ground vehicle," *IEEE/ASME Transactions on Mechatronics*, vol. 26, no. 1, pp. 33–44, 2020.

[5] J. Guo, J. Wang, Y. Luo, and K. Li, "Takagi–sugeno fuzzy-based robust H∞ integrated lane-keeping and direct yaw moment controller of unmanned electric vehicles," *IEEE/ASME Transactions on Mechatronics*, vol. 26, no. 4, pp. 2151–2162, 2020.

[6] B-M. Nguyen, M. Kawanishi, D. Hasegawa, K. Ohara, and T. Narikiyo, "Range extension control of a three-wheel electric vehicle prototype based on aggregation and distribution," *IEEJ Journal of Industry Applications*, vol. 10, no. 5, pp. 528–539, 2021.

[7] D. A. de Lima and A. C. Victorino, "A visual servoing approach for road lane following with obstacle avoidance," in *17th International IEEE Conference on Intelligent Transportation Systems (ITSC)*. IEEE, 2014, pp. 412–417.

[8] Y. Hori, Y. Toyoda, and Y. Tsuruoka, "Traction control of electric vehicle: basic experimental results using the test ev" uot electric march"," *IEEE transactions on Industry Applications*, vol. 34, no. 5, pp. 1131–1138, 1998.

[9] H. Fujimoto, T. Saito, A. Tsumasaka, and T. Noguchi, "Motion control and road condition estimation of electric vehicles with two in-wheel motors," in *Proceedings of the 2004 IEEE International Conference on Control Applications, 2004.*, vol. 2. IEEE, 2004, pp. 1266–1271.

[10] B-M. Nguyen, S. Hara, H. Fujimoto, and Y. Hori, "Slip control for iwm vehicles based on hierarchical lqr," *Control Engineering Practice*, vol. 93, p. 104179, 2019.

[11] P. Khatun, C. M. Bingham, N. Schofield, and P. Mellor, "Application of fuzzy control algorithms for electric vehicle antilock braking/traction control systems," *IEEE Transactions on Vehicular Technology*, vol. 52, no. 5, pp. 1356–1364, 2003.

[12] Y. Ma, J. Zhao, H. Zhao, C. Lu, and H. Chen, "Mpc-based slip ratio control for electric vehicle considering road roughness," *IEEE Access*, vol. 7, pp. 52 405–52 413, 2019.

[13] D. Savitski, V. Ivanov, K. Augsburg, T. Emmei, H. Fuse, H. Fujimoto, and L. M. Fridman, "Wheel slip control for the electric vehicle with in-wheel motors: Variable structure and sliding mode methods," *IEEE Transactions on Industrial Electronics*, vol. 67, no. 10, pp. 8535–8544, 2019.

[14] J. Amada and H. Fujimoto, "Torque based direct driving force control method with driving stiffness estimation for electric vehicle with in-wheel motor," in *IECON 2012-38th Annual Conference on IEEE Industrial Electronics Society*. IEEE, 2012, pp. 4904–4909.

[15] K. Maeda, H. Fujimoto, and Y. Hori, "Four-wheel driving-force distribution method based on driving stiffness and slip ratio estimation for electric vehicle with in-wheel motors," in *2012 IEEE vehicle power and propulsion conference*. IEEE, 2012, pp. 1286–1291.

[16] Y. Chen and J. Wang, "Adaptive vehicle speed control with input injections for longitudinal motion independent road frictional condition estimation," *IEEE Transactions on Vehicular Technology*, vol. 60, no. 3, pp. 839–848, 2011.

[17] K. Berntorp and S. Di Cairano, "Tire-stiffness and vehicle-state estimation based on noise-adaptive particle filtering," *IEEE Transactions on Control Systems Technology*, vol. 27, no. 3, pp. 1100–1114, 2018.

[18] D. Jin, B. Leng, X. Yang, L. Xiong, and Z. Yu, "Road friction estimation method based on fusion of machine vision and vehicle dynamics," in *2020 IEEE Intelligent Vehicles Symposium (IV)*. IEEE, 2020, pp. 1771–1776.

[19] S. Roychowdhury, M. Zhao, A. Wallin, N. Ohlsson, and M. Jonasson, "Machine learning models for road surface and friction estimation using front-camera images," in *2018 International Joint Conference on Neural Networks (IJCNN)*. IEEE, 2018, pp. 1–8.

[20] L. Cheng, X. Zhang, and J. Shen, "Road surface condition classification using deep learning," *Journal of Visual Communication and Image Representation*, vol. 64, p. 102638, 2019. [Online]. Available: https://www.sciencedirect.com/science/article/pii/S1047320319302597

[21] L. Alzubaidi, J. Zhang, A. J. Humaidi, A. Al-Dujaili, Y. Duan, O. Al-Shamma, J. Santamaria, M. A. Fadhel, M. Al-Amidie, and L. Farhan, "Review of deep learning: Concepts, cnn architectures, challenges, applications, future directions," *Journal of big Data*, vol. 8, no. 1, pp. 1–74, 2021.

[22] E. Oguz, A. Küçükmanisa, R. Duvar, and O. Urhan, "A deep learning based fast lane detection approach," *Chaos, Solitons & Fractals*, vol. 155, p. 111722, 2022. [Online]. Available: https://www.sciencedirect.com/science/article/pii/S0960077921010766

[23] Y. Ma, S. Soatto, J. Kosecka, and S. Sastry, *An invitation to 3-d vision: from images to geometric models*. Springer, 2004, vol. 26.

[24] H. B. Pacejka and E. Bakker, "The magic formula tyre model," *Vehicle system dynamics*, vol. 21, no. S1, pp. 1–18, 1992.

ACKNOWLEDGMENT

This project has received funding from the European Commission under the H2020 Grant agreement OWHEEL No.872907.

This research was also partly supported by Industrial Technology Research Grant Program from New Energy and Industrial Technology Development Organization (NEDO) of Japan (number 05A48701d), the Ministry of Education, Culture, Sports, Science and Technology grant (number 22246057 and 26249061), and by the European Commission under the H2020 Grant agreement OWheel (number 872907).